

# A generalized approach to parallel magnetic resonance imaging

Daniel K. Sodickson<sup>a)</sup> and Charles A. McKenzie

Department of Medicine, Cardiovascular Division, Beth Israel Deaconess Medical Center  
and Harvard Medical School, Boston, Massachusetts

(Received 4 December 2000; accepted for publication 30 May 2001)

Parallel magnetic resonance (MR) imaging uses spatial encoding from multiple radiofrequency detector coils to supplement the encoding supplied by magnetic field gradients, and thereby to accelerate MR image acquisitions beyond previous limits. A generalized formulation for parallel MR imaging is derived, demonstrating the relationship between existing techniques such as SMASH and SENSE, and suggesting new algorithms with improved performance. Hybrid approaches combining features of both SMASH-like and SENSE-like image reconstructions are constructed, and numerical conditioning techniques are described which can improve the practical robustness of parallel image reconstructions. Incorporation of numerical conditioning directly into parallel reconstructions using the generalized approach also removes a cumbersome and potentially error-prone sensitivity calibration step involving division of two distinct *in vivo* reference images. Hybrid approaches in combination with numerical conditioning are shown to extend the range of accelerations over which high-quality parallel images may be obtained. © 2001 American Association of Physicists in Medicine. [DOI: 10.1118/1.1386778]

Key words: rapid imaging, parallel MRI, SMASH, SENSE

## I. INTRODUCTION

Imaging speed is of critical importance in many clinical applications of magnetic resonance imaging. Imaging of the cardiovascular system, for example, must contend with the challenges of cardiac motion, respiratory motion, and blood flow. Improvements in MR image acquisition speed over the past decade have allowed significant advances in the visualization and characterization of moving structures. Nevertheless, physical and physiologic constraints on the switching rate of magnetic field gradients and radiofrequency (RF) pulses place certain basic limits on the speed of traditional MR image acquisitions. Many modern MR scanners already operate close to these limits.

In the course of the past decade, a new approach to MR image acquisition has been developed, which can extend or circumvent the speed limits traditionally associated with gradient and RF hardware. This approach, known as “parallel MRI,” uses spatial information from arrays of RF coils to perform some portion of the spatial encoding normally accomplished using gradients and RF pulses.<sup>1</sup> The effective use of multiple detectors in parallel has been shown to multiply imaging speed, without increasing gradient switching rate or RF power deposition.

This paradigm of parallel MRI has evolved rapidly in the past few years. Following a number of early proposals for parallel imaging,<sup>2–7</sup> accelerated *in vivo* images were published in 1997 using the Simultaneous Acquisition of Spatial Harmonics (SMASH) technique.<sup>8</sup> SMASH uses linear combinations of component coil signals to emulate directly the effects of encoding gradients, and thereby to reduce the number of time-consuming gradient steps required for image formation. Sinusoidal spatial modulations, or “spatial harmonics,” are formed by linear combination of measured

component coil sensitivities, and the same linear combinations are applied to component coil signals in order to generate shifted composite MR signals which can take the place of omitted gradient steps.<sup>8–10</sup>

Subsequent to the introduction of SMASH, the SENSitivity Encoding (SENSE) technique was developed and was also applied successfully to *in vivo* imaging.<sup>11</sup> The SENSE formalism generalized various features of earlier proposed approaches,<sup>4,7</sup> extending the theory to accommodate arbitrary *k*-space trajectories, including consideration of reconstructed voxel shapes, and also introducing a several-stage postprocessing algorithm to smooth and normalize measured coil sensitivities. In its most common implementations for regularly sampled MR signal data, the SENSE reconstruction operates on component coil images following Fourier transformation, using measured sensitivity calibration information to “unfold” the Nyquist-aliased images which result from omission of gradient steps.

In the past few years, a wide range of imaging applications have been explored using SMASH and SENSE.<sup>8–19</sup> Meanwhile, various alternative parallel MRI techniques are beginning to be developed.<sup>20–25</sup> These new techniques in general tend to resemble either the SMASH or the SENSE approach, and comparisons or connections between the two basic approaches have been the subject of discussion and speculation for some time.

This article outlines a generalized formulation which may be used to understand and to exploit the connections between various parallel imaging techniques. The generalized approach allows direct comparison of the SMASH-like and SENSE-like classes of techniques, and provides insight into the origins of some of their distinct practical features. Once the problem of parallel image reconstruction has been suitably formulated, appropriate basis transformations and other

linear algebraic tools are used not only to derive the most common implementations of SMASH or SENSE as special cases, but also to design new reconstruction approaches with distinct and useful properties.

For example, appropriate modification of parameters in the generalized approach allows the generation of hybrid techniques combining some of the advantages of SMASH-like and SENSE-like approaches.<sup>26</sup> Furthermore, numerical conditioning approaches are incorporated naturally and conveniently into the generalized formalism. This important feature of numerical conditioning enables effective compensation for noise or for systematic errors in coil sensitivity calibration, resulting in improved image quality and signal-to-noise ratio (SNR) under a wide range of conditions. In short, the generalized approach described here not only provides a unifying perspective connecting various parallel imaging techniques, but, in combination with appropriate numerical conditioning approaches, it also allows substantive improvements to techniques such as SMASH and SENSE.

## II. THEORY

We begin with the recognition that measured MR signal data comprise a generalized series of projections of the underlying distribution of MR-active spins in the imaged volume. A listing of the various projection functions then leads to practical strategies for parallel image reconstruction.

The MR signal from an arbitrary two-dimensional slice detected in any given RF coil is the result of a spatial integration of spin density  $\rho$  against the sensitivity  $C_l$  of that coil in the plane of the slice and against the sinusoidal spatial modulations generated by encoding gradients:

$$S_l(k_x, k_y) = \int \int dx dy C_l(x, y) \times \exp(-ik_x x) \exp(-ik_y y) \rho(x, y). \quad (1)$$

Here,  $l = 1, 2, \dots, L$  is the index of any component coil in an  $L$ -coil array, and  $k_x$  and  $k_y$  are the  $k$ -space indices representing a total of  $N_x$  and  $N_y$  different measured time evolutions in the presence of frequency and phase-encoding gradients. In other words, the signal comprises integrations or projections of the spin density against  $L \cdot N_x \cdot N_y$  distinct functions:

$$B_l(x, y, k_x, k_y) = C_l(x, y) \exp(-ik_x x) \exp(-ik_y y). \quad (2)$$

These functions will be referred to herein as “encoding functions,” since they represent a method by which spatial encoding may be performed. Figure 1 shows the composition of some sample encoding functions for a single surface coil and several phase encoding gradient steps. Specifically, as shown in Fig. 1, an encoding function is formed by superimposing the coil sensitivity modulation on a gradient modulation. For example, in the top row of Fig. 1, the coil sensitivity modulation is multiplied by a constant function corresponding to a zero gradient amplitude. Thus, the first encoding function is the coil sensitivity modulation itself. In the second row, the coil sensitivity modulation is multiplied by the first spatial harmonic to form a second encoding function. Numerous other encoding functions may likewise be

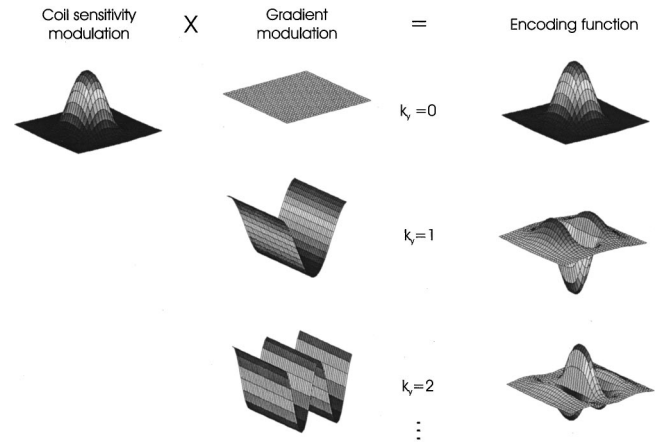


FIG. 1. Encoding functions composed of coil sensitivity modulations and gradient modulations.

formed. For simplicity, only the real parts of the various functions are shown in Fig. 1. In practice, coil sensitivities and gradient modulations alike will have both real and imaginary components, as will the encoding functions formed from their products. For convenience, the effects of relaxation have also been ignored in Eqs. (1) and (2) and Fig. 1. They may be included by making the simple substitution

$$C_l(x, y) \rightarrow C_l(x, y) R(x, y, k_x, k_y), \quad (3)$$

where  $R(x, y, k_x, k_y)$  is a function representing the relaxation-induced variations in signal intensity as a function of time (or, equivalently, of  $k$ -space index) at each position in the imaged volume.

The encoding functions in Fig. 1 may be said to represent different “views” of the image to be reconstructed, with each measured signal point representing the projected appearance of the image from the corresponding “view.” From this perspective, parallel MR image reconstruction, and MR image reconstruction in general, bears an analogy to x-ray computed tomography, in which an estimate of image intensity is generated from a (frequently overdetermined) set of distinct measured projections, using the apparatus of linear algebra. Figure 2 illustrates this analogy schematically. In CT imaging, an x-ray emitter (or an array of emitters) sends x-ray beams through the imaged volume, and attenuated beam intensities are recorded in a detector or detector array. The measured x-ray intensities represent integrations of beam attenuation along the beam path, or, in other words, projections of the distribution of attenuators along the path. Rotation of the beam direction (coupled with translation and/or with fan-beam geometry) yields the requisite number of projections, from which a full 2D image of the area of interest may be generated. In MR imaging, a body coil or other suitable transmission coil takes the place of the x-ray emitter, detection is performed in an RF coil or coil array, and field gradients are switched, in lieu of gantry rotation, to yield projections against the corresponding encoding functions. The

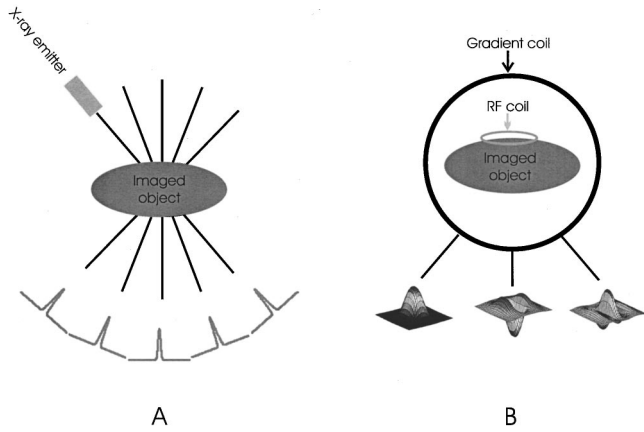


FIG. 2. Schematic representation of generalized projections in x-ray computed tomography (a) and magnetic resonance imaging (b).

particular projections may differ between the modalities, but, from this broad perspective, the overall problem of image reconstruction is the same.

We may now apply the tools of linear algebra to the MR reconstruction problem in the presence of multiple RF coils. With only a modest loss of generality, the integral in Eq. (1) may be approximated with a discrete sum. The implications of different strategies of discretization, as well as generalizations to the continuous case, are discussed in the Appendix; for now, let us assume that the coil sensitivity profiles and gradient modulations which make up the encoding functions in Eq. (2) may be represented by discrete functions sampled at well-defined spatial positions. Equation (1) may then be written as follows, using a single  $k$ -space index  $k = (k_x, k_y)$  for the  $N = N_x^* N_y$   $k$ -space samples, and a corresponding single pixel index  $j = (x, y)$  for the various pixel positions:

$$S_l(k_x, k_y) \equiv S_{kl} \approx \sum_j C_{jl} \exp(-2\pi i j k / N) \rho_j \equiv \sum_j B_{klj} \rho_j. \quad (4)$$

For any given coil  $l$ , this is just a discrete Fourier transform (DFT), which is easily inverted with an inverse DFT:

$$C_{jl} \rho_j \approx \frac{1}{N} \sum_k S_{kl} \exp(2\pi i j k / N). \quad (5)$$

However, the signals from all the coils in the array may also be grouped together into a single index  $p = (k, l)$ , yielding the following matrix equation,

$$S_p \approx \sum_j B_{pj} \rho_j, \quad (6)$$

or, in matrix notation,

$$\mathbf{S} = \mathbf{B} \boldsymbol{\rho}. \quad (7)$$

Inverting this equation yields an expression for the spin density alone:

$$\boldsymbol{\rho} = \mathbf{B}^{-1} \mathbf{S}. \quad (8)$$

In other words, if  $\mathbf{B}^{-1}$  can be calculated, the spin density can be determined.

The encoding matrix  $\mathbf{B}$  is constructed as an ordered list of the various encoding functions made up of coil sensitivity modulations and gradient modulations. If a complete set of  $N_x^* N_y$  gradient evolutions are sampled, corresponding to  $N_x^* N_y$  pixels in the reconstructed image, the  $\mathbf{B}$  matrix has dimension  $(N_x^* N_y^* L) \times (N_x^* N_y)$ . This is clearly overdetermined. Encoding gradient steps may be omitted up to a maximum factor of  $L$ , and  $\mathbf{B}$  will remain invertible in principle. In other words, when spatial information from an array of coils is available, the spin density may be determined from a reduced set of encoding gradients. This is the basis of spatial encoding in parallel imaging.

For image acquisitions of appreciable matrix size, the dimension of  $\mathbf{B}$  is large, and brute force inversion may be quite time-consuming and memory-intensive. If, however, the acquisition involves a regular Cartesian sampling of  $k$ -space, a Fourier transform may be performed along any non-coil-encoded directions (e.g., the frequency-encoding direction in typical applications), and the  $\mathbf{B}$  matrix then attains a block diagonal structure which can substantially simplify its processing. Rewriting Eq. (4) in terms of  $k$ -space indices  $k_x$  and  $k_y$  in two orthogonal directions, and performing an inverse DFT along the  $x$  direction (taken to be the frequency-encoding direction) gives

$$\begin{aligned} \hat{S}_l(x, k_y) &\equiv \text{DFT}_x^{-1} \left( \sum_{x'} \sum_y C_{x'y l} \exp(-2\pi i k_x x') \right. \\ &\quad \left. \times \exp(-2\pi i k_y y) \rho_{x', y} \right) \\ &= \frac{1}{N_x} \sum_{k_x} \exp(2\pi i k_x x) \sum_{x'} \sum_y C_{x'y l} \\ &\quad \times \exp(-2\pi i k_x x') \exp(-2\pi i k_y y) \rho_{x', y} \\ &= \sum_{x'} \sum_y C_{x'y l} \delta_{x'x} \exp(-2\pi i k_y y) \rho_{x', y} \\ &= \sum_y C_{xy l} \exp(-2\pi i k_y y) \rho_{x, y}. \end{aligned} \quad (9)$$

[In order to distinguish the summation over  $x$  in the raw signal from the position label  $x$  in the transformed signal, a dummy variable  $x'$  has been used for the internal summation in Eq. (9).] A transformed  $\mathbf{B}$  matrix may now be defined as follows:

$$\hat{B}_{(xk_y l), (x' y)} \equiv \delta_{x'x} C_{xy l} \exp(-2\pi i k_y y) \equiv \delta_{x'x} \hat{B}_{(k_y l), (y)}^{(x)}, \quad (10)$$

and the spin density may be determined from a transformed matrix equation:

$$\rho_{x, y} = \sum_{p=(k_y, l)} (\hat{B}^{(x)})_{yp}^{-1} \hat{S}_{px}. \quad (11)$$

The delta function in Eq. (10) indicates that the transformed encoding matrix is block diagonal in the  $x$  and  $x'$  indices [which constitute subsets of the row and column indices of the matrix, which takes  $(x, k_y, l)$  into  $(x', y)$ ]. Thus,

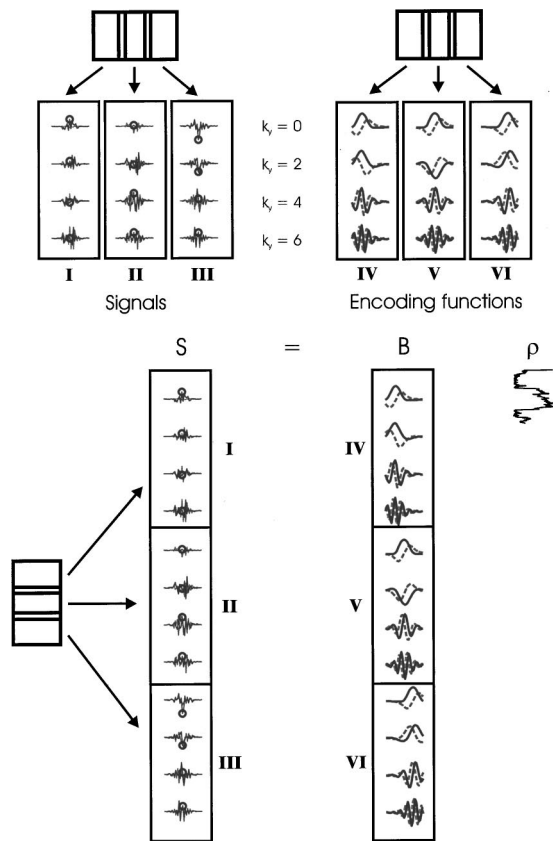


FIG. 3. Construction of the signal vector and encoding matrix in Eq. (7). Signals from each component coil (I, II, III) at each phase-encoding gradient step are grouped into a signal vector  $S$  for each frequency-encoding position (one sample position indicated by circles). The corresponding encoding functions (IV, V, VI) are grouped into an encoding matrix  $B$ , which must be inverted to reconstruct the spin density  $\rho$ . Both real (solid lines) and imaginary (dashed lines) parts of the encoding functions are shown.

the reconstruction may proceed line by line for each position in the frequency-encoding direction, using an encoding matrix made up of coil sensitivity and gradient modulations taken only along each line. Instead of an  $(N_x N_y L/M) \times (N_x N_y)$ -dimensional inverse (assuming an undersampling in the phase-encoding direction by a factor of  $M$ ), the reconstruction problem has been reduced to a total of  $N_x$  inversions each of dimension  $(N_y L/M) \times (N_y)$ . For simplicity and ease of visualization, we will use the special case of a block-diagonalized line-by-line reconstruction, in which the first Fourier transform has been performed as in Eq. (9), to illustrate the construction and inversion of the transformed encoding matrix. Generalization to the case of the full encoding matrix is straightforward.

The structure of the transformed  $B$  matrix, and the procedure by which its entries are filled, is indicated graphically for an illustrative case in Fig. 3. At the top right of the figure, encoding functions are shown for each of three component coils and four phase encoding gradient steps (with intermediate phase encoding steps deliberately omitted for subsequent parallel reconstruction). Real and imaginary parts of the encoding functions are indicated by solid and dashed lines, respectively. The corresponding measured signal lines

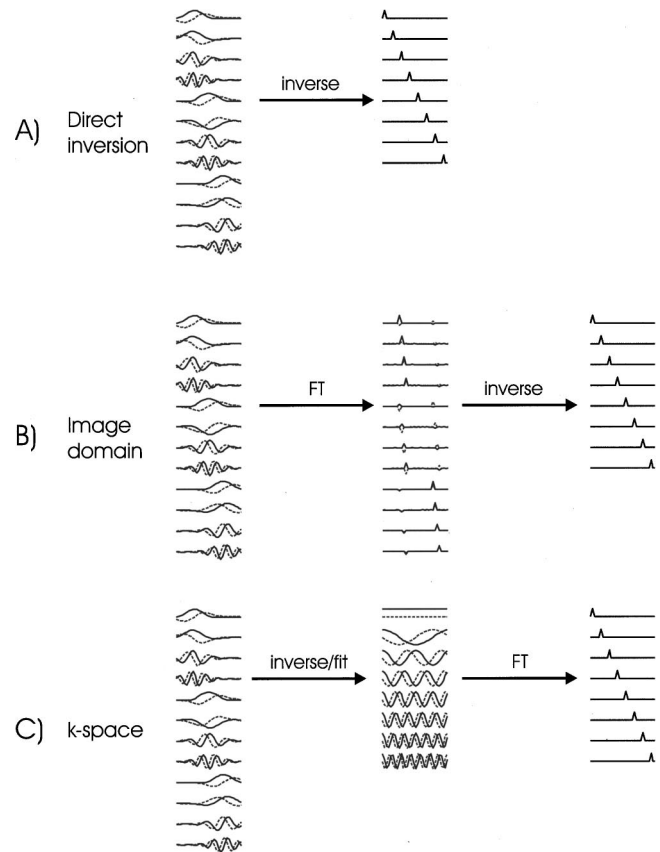


FIG. 4. Various encoding matrix inversion strategies. (a) Direct inversion. (b) Image-domain reconstruction, in which a Fourier transform (FT) precedes matrix inversion. (c)  $k$ -space reconstruction, in which the FT follows a basis transformation or spatial harmonic fitting procedure involving a matrix inversion. Real (solid lines) and imaginary (dashed lines) parts of the encoding functions grouped into encoding matrices as in Fig. 3 are shown at left.

(Fourier-transformed in the frequency-encoding direction) are shown at the top left. The circles on the signal plots are intended to indicate that one frequency-encoding position at a time is selected, and the encoding functions at right apply only for that one position. The bottom of Fig. 3 has the structure of Eq. (7), and demonstrates how the signals and encoding functions are grouped (in blocks identified by roman numerals) to form the signal vector and the  $B$  matrix for each frequency-encoding position.

The encoding  $B$  matrix may be inverted, and the reconstruction thereby accomplished, in a number of ways. Figure 4 illustrates three different strategies for  $B$  matrix inversion. Figure 4(a) shows a direct inversion, which may be performed using a suitable generalized inverse procedure such as the Moore–Penrose pseudoinverse.<sup>27</sup> The result of the generalized inverse is a matrix which when multiplied by  $B$  generates an identity matrix (shown as a set of shifted delta functions corresponding to a unit diagonal) with the correct dimension for the reconstructed data set. Alternatively, the rows of the  $B$  matrix as shown in Fig. 4(a) may be said to represent  $3 \times 4 = 12$  vectors in an eight-dimensional space, and the inverse is a matrix that converts these vectors to a basis of eight orthogonal (delta function) vectors spanning the



space. Operation of the inverse on the ordered signal vector  $\mathbf{S}$  will then generate the reconstructed pixel values directly, without need for a separate Fourier transform. That is, the normally required FT is included in the inversion.

The strategies shown in Figs. 4(b) and 4(c) involve separating out the Fourier transform as a distinct step, and combining it in varying order with an inverse or a related basis transformation. The sections to follow will show that the image-domain reconstruction techniques such as SENSE and the  $k$ -space reconstruction techniques such as SMASH may be identified with the inversion strategies in Figs. 4(b) and 4(c), respectively. Hybrid approaches will then be designed by applying various constraints to the inversion.

### A. Image-domain reconstructions: The pixel basis

An additional Fourier transform of Eq. (9) along the phase encoding direction ( $y$ ) completes the transformation of measured MR signal into the image domain. In a fully sampled gradient-encoded acquisition, this additional Fourier transform applied to the  $\mathbf{B}$  matrix would yield a diagonal matrix of shifted delta functions for each component coil, corresponding to the coil sensitivities at various pixel positions.

Due to the undersampling of  $k$ -space in the phase-encoding direction, however, the FT along that direction yields multiple nonzero values in each row of the transformed matrix. This is the result of Nyquist aliasing. For the particular case of a  $k$ -space sampling trajectory corresponding to a regular Cartesian grid, with undersampling by a factor of  $M$ ,  $\mathbf{B}$  transforms to a sparse multidagonal matrix, as shown in Fig. 4(b) for  $M=2$ . Formally,

$$\begin{aligned}\hat{S}_l(x, y) &\equiv \text{DFT}_y^{-1}(\hat{S}_l(x, k_y)) \\ &= \frac{1}{(N_y/M)} \sum_{k_y=0, M, 2M, \dots} \exp(2\pi i k_y y) \\ &\quad \times \sum_{y'} C_{xy'l} \exp(-2\pi i k_y y') \rho_{x, y'} \\ &= \sum_{y'} \sum_{m=0}^{M-1} \delta_{y', y+m N_y/M} C_{xy'l} \rho_{x, y'} \\ &\equiv \sum_{y'} \hat{B}_{(yl), y'}^{(x)} \rho_{x, y'} = \sum_{m=0}^{M-1} C_{x, y+m N_y/M, l} \rho_{x, y+m N_y/M} \\ &\equiv \sum_{m=0}^{M-1} \hat{C}_{lm}^{(x)} \rho_{x, y+m N_y/M}.\end{aligned}\quad (12)$$

Once again, as in Eq. (9), a dummy index ( $y'$ ) has been used to represent the internal spatial summation. Unlike in Eq. (9), however, summation over a reduced set of  $k_y$  values fails to produce complete destructive interference at several intermediate spatial positions across the field of view (FOV), resulting in multiple delta functions at  $y + m N_y/M$ , where  $m$  is an integer,  $M$  is the undersampling factor, and  $N_y$  is the spatial index corresponding to the edge of the FOV in the  $y$  direc-

tion. Through the action of these multiple delta functions, spatial positions separated by an appropriate fraction of the FOV are connected by aliasing.

The matrix  $\hat{B}_{(yl), y'}^{(x)}$  may be inverted using sparse matrix techniques, or else it may be reordered into block diagonal form as in the last line of Eq. (12), yielding a distinct  $(L \times M)$ -dimensional inversion for each pixel position in the reconstructed image:

$$\rho_{x, y+m N_y/M} = \sum_l (\hat{C}^{(x)})_{ml}^{-1} \hat{S}_{lxy}. \quad (13)$$

Each block then corresponds to a set of aliased pixels, and the inversion corresponds to the pixel by pixel inversion used in the subencoding technique<sup>4,7</sup> or in typical implementations of SENSE.<sup>11</sup> From the perspective of basis transformations, the overdetermined set of differently aliased pixel values is mapped to a set of unaliased pixel values which spans the vector space of the image.

### B. $k$ -space reconstructions: The Fourier basis

The  $\mathbf{B}$  matrix may be transformed to bases other than the delta function pixel basis. Figure 4(c) shows such a transformation, where the target basis is made up of orthogonal sinusoidal modulations—or, in other words, of spatial harmonics. In the example shown in Fig. 4(c), the missing harmonics associated with  $k_y$ -space positions  $k_y=1, 3, 5, 7$  have been filled in to form the full target harmonic basis. Fourier transformation in the phase-encoding direction will then yield the fully encoded image, with no aliasing. This is an example of a  $k$ -space reconstruction, in which the bulk of the processing occurs prior to Fourier transformation, and in which the final inverse FT is performed on the composite data rather than on each component coil data set separately. Since the basis transformation in general involves some form of generalized inverse or fitting procedure, this step is labeled “inverse/fit” in Fig. 4(c).

The procedure of Fig. 4(c), as it stands, is not yet fully equivalent to the SMASH image reconstruction. One further simplification is required to achieve complete equivalence to SMASH. Figure 5 demonstrates this simplification. If the entries in the  $\mathbf{B}$  matrix are first permuted so as to group the encoding functions associated with all the component coils together for any given gradient step, the topmost boxed entries in the transformation take the familiar form of the canonical SMASH fit which maps coil sensitivities to spatial harmonics.

In fact, the SMASH reconstruction is accomplished by inverting only this small subblock of the full  $\mathbf{B}$  matrix, and applying the resulting transformation identically to all remaining subblocks. Thus, the approximation inherent in the SMASH spatial harmonic fit may be understood as a reduction of the effective dimensionality of the encoding matrix. This reduction of dimensionality is a central point of divergence between the SMASH reconstruction and typical image domain reconstructions such as subencoding or SENSE.

One reason that the SMASH approximation is often valid, as evidenced by the success of SMASH reconstructions in

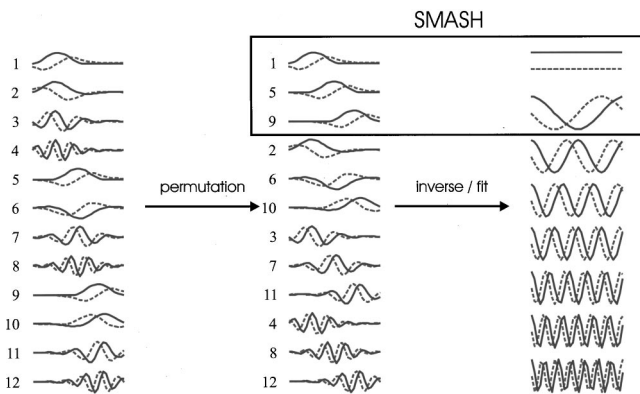


FIG. 5. Derivation of the SMASH spatial harmonic fit as inversion of a subblock of the full encoding matrix. Permutation of the rows of the encoding matrix from Fig. 4(c) results in a fitting problem whose topmost block (solid rectangle) corresponds to the SMASH fitting procedure.

practice,<sup>8-10,12-17</sup> stems from the repeating block structure of the **B** matrix. If the shape of the sensitivities permits a perfect fit of the lowest-order target spatial harmonics for the single SMASH subblock, then the fits will also be perfect for all additional subblocks, since these subblocks and target harmonics are both simply harmonic multiples of the first set. Thus, in this situation, there is no need to cross subblocks to correct an already perfect fit.

Of course, spatial harmonic fits are not, in general, truly perfect. Even when pure harmonic fits begin to degrade, however, tailored fits may still be used, as described in Ref. 10, to achieve high degrees of accuracy, for example in highly oblique image planes. Tailored harmonic fitting simply corresponds to multiplying all target harmonics by a common function which makes the fit both more accurate and better conditioned.<sup>10</sup>

As the fit improves, the various subblocks of the encoding matrix become more effectively isolated, and the SMASH approximation thus introduces only insignificant errors. Additionally, the influence of certain other practical sources of error are diminished. Since the effective dimensions of the **B** matrix are reduced and the various subblocks are isolated from each other in SMASH, the reconstruction is prevented from “overcorrecting” for pixel-by-pixel inaccuracies due to sensitivity calibration errors or noise. Thus, the SMASH approximation can serve to alleviate potential numerical instabilities which may result in practice from inversion of the larger matrix. Additionally, since only a small subblock of the encoding matrix must be inverted, image reconstruction times can be significantly reduced.

### C. Hybrid reconstructions

The optimal choice of parallel reconstruction strategy, whether in *k*-space or in the image domain, will be determined by practical constraints of the **B** matrix inversion in each strategy—its accuracy, its noise and error propagation characteristics, the processing time required, etc. In many cases, it may be desirable to trade off some of these features against others. Using the generalized formalism outlined so

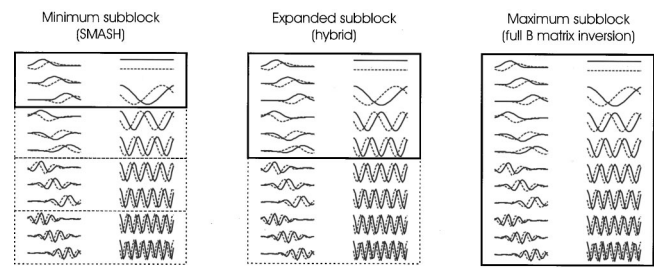


FIG. 6. Various encoding matrix subblock sizes (solid rectangles), corresponding to SMASH (left), full **B** matrix inversion (right), or an intermediate expanded subblock hybrid reconstruction (center).

far, it is possible to form hybrid reconstruction strategies which combine some of the features and advantages of the SMASH-like and the SENSE-like techniques.

One type of hybrid reconstruction is naturally suggested by the subblock structure of the SMASH reconstruction in Fig. 5. If properties intermediate between SMASH and full **B** matrix inversions such as subencoding or SENSE are desired, the size of the inverted subblock may be expanded, as is shown schematically in Fig. 6.

Figure 6(a) shows a **B** matrix inverted using the minimum-size subblock, corresponding to a SMASH procedure. Figure 6(b) illustrates a hybrid reconstruction formed by choosing an expanded subblock, including not only the pure sensitivities but also the second-harmonic-modulated encoding functions. This procedure may also be understood as an expanded spatial harmonic fit, in which a larger number of effective “sensitivities” (represented by the various encoding functions) are fitted to a correspondingly wider range of target harmonics. Figure 6(c) illustrates the largest possible subblock, corresponding to inversion of the full **B** matrix, which, as discussed above, is in principle equivalent to an image domain subencoding or SENSE reconstruction.

The expanded subblock approach can thus be used to scale smoothly from a SMASH-equivalent reconstruction to an image-domain-equivalent reconstruction. Since a typical image acquisition involves far more than the four phase-encoding gradient steps represented in Fig. 6, a wide range of subblock sizes will be available.

Figure 7 compares sixfold accelerated images of a phantom reconstructed using a minimum subblock size (a), an intermediate subblock size of 7 times minimum (b), and a full block size of 21 times minimum (c). An unaccelerated reference image formed as the square root of the sum of squares of fully gradient-encoded component coil images<sup>28</sup> is included in Fig. 7(d). Due to the high acceleration (a maximal factor of 6 for a six-element array) and the large double-oblique angulation of the image plane, the full encoding matrix inversion in Fig. 7(c) suffers from numerical instabilities, which manifest as discrete point-wise artifacts obscuring the structure of the phantom. By contrast, the minimum-subblock SMASH inversion in Fig. 7(a), though theoretically less accurate than the full inversion, controls these instabilities and results in a clearer depiction of the phantom. The expanded subblock hybrid in Fig. 7(b) has properties inter-

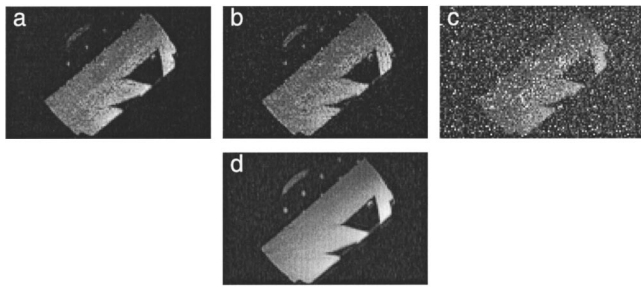


FIG. 7. (a)–(c) Sixfold accelerated double-oblique images of a phantom reconstructed using a minimum subblock size of one encoding function per array element (a), an intermediate subblock size of 7 times minimum (b), and a full block size of 21 times minimum (c). (d) Unaccelerated reference image formed as the square root of the sum of squares of fully gradient-encoded component coil images. Image data were acquired using a gradient echo imaging sequence (TR=21 ms, TE=2.1 ms, matrix size=126×128 for unaccelerated reference and 21×128 reconstructed to 126×128 for accelerated images, FOV=300×300 mm<sup>2</sup> for unaccelerated reference and 50×300 mm<sup>2</sup> reconstructed to 300×300 mm<sup>2</sup> for accelerated images, slice thickness=2 mm) with a six-element coil array on a Philips NT 1.5T imaging system (Philips Medical Systems, Best, The Netherlands). A separate acquisition with the same sequence and coil array was used for a sensitivity reference.

mediate between the reconstructions in Figs. 7(a) and 7(c).

Intermediate hybrid reconstructions, such as the one shown in Fig. 7(b), thus share some of the numerical stability and efficiency of the SMASH technique, while also allowing some of the theoretical accuracy inherent in the image-domain techniques. The element of approximation is progressively reduced as the subblock is expanded, which may be useful in cases for which a pure SMASH reconstruction shows an undesirable level of residual aliasing artifacts.

In the expanded subblock fits, the independence of the various encoding function sets is relaxed, so that corrections from higher-frequency encoding functions may be used to improve the basic SMASH fit, and more accurate spatial harmonics may be generated. On the other hand, expansion of the subblock will increase reconstruction time, and sacrifice some of the protection against “overcorrection” for localized noise and calibration errors. In addition, larger blocks of  $k$ -space lines must be collected prior to combination in an expanded subblock reconstruction, so that the reconstruction

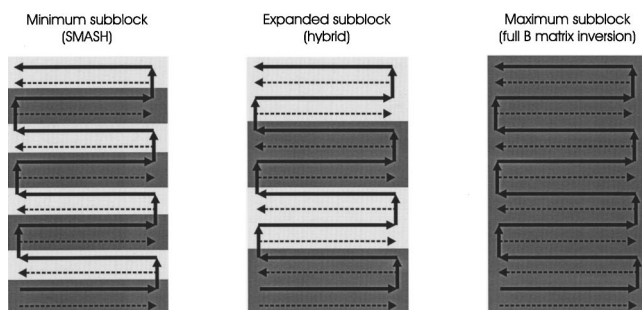


FIG. 8. The grouping of  $k$ -space lines for various encoding matrix subblock sizes in a schematic twofold accelerated acquisition. Solid lines: acquired  $k$ -space lines. Dashed lines: additional  $k$ -space lines reconstructed by encoding matrix inversion. All reconstructed lines in each alternating light or dark gray band are generated using only the acquired lines in the same band.

becomes more cumbersome to implement in real time than the pure SMASH reconstruction, which may in principle be performed as each point or line of  $k$ -space is acquired in the scanner.

Figure 8 shows the grouping of  $k$ -space lines for which separate combinations are formed in sample subblock reconstructions. Thick solid lines represent acquired data lines (in a schematic echo-planar-style  $k$ -space trajectory), and thinner dashed lines represent data lines to be filled in by parallel reconstruction. As the subblock is expanded, larger groups of acquired  $k$ -space lines (grouped by alternately shaded backgrounds) are combined to form correspondingly larger sets of reconstructed lines. Thus, the flexibility of the expanded subblock hybrid approach does come at some price in computational complexity and reconstruction time, but the added flexibility may frequently be worth the price in practical imaging situations.

#### D. Numerical conditioning in practical encoding matrix inversions

Now that we have explored some of the structure of the encoding matrix in its various incarnations, let us turn to the properties of its inverse, which must ultimately be formed in order to reconstruct an image. The generalized inverse of a nonsquare matrix is not uniquely defined,<sup>29</sup> thus we are free to choose an inverse with desirable properties. One such inverse is the Moore–Penrose pseudoinverse,<sup>27</sup> which may be accomplished in several ways. If the inverse of the square matrix  $\mathbf{B}^T \mathbf{B}$  exists, the following standard formula may be used for the Moore–Penrose pseudoinverse:

$$\mathbf{B}_{\text{pseudo}}^{-1} = (\mathbf{B}^T \mathbf{B})^{-1} \mathbf{B}^T. \quad (14)$$

The symbol  $^T$  represents a conjugate transpose, or Hermitian transpose. Alternatively, a singular value decomposition (SVD) of the  $\mathbf{B}$  matrix may be formed,

$$\mathbf{B} = \mathbf{U} \mathbf{D} \mathbf{V}^T, \quad (15)$$

where  $\mathbf{U}$  and  $\mathbf{V}$  are unitary matrices and  $\mathbf{D}$  is a diagonal matrix containing non-negative diagonal elements in order of decreasing size. The Moore–Penrose pseudoinverse may then be calculated as

$$\mathbf{B}_{\text{pseudo}}^{-1} = \mathbf{V} \mathbf{D}^{-1} \mathbf{U}^T, \quad (16)$$

where  $\mathbf{D}^{-1}$  is a transposed diagonal matrix containing the inverses of the nonzero diagonal elements of  $\mathbf{D}$ .

It was mentioned earlier that the basis transformations involved in  $k$ -space reconstructions [Fig. 4(c)] involved a generalized inverse procedure. This is trivial to see if the basis transformation is formulated as a generalized fitting problem

$$\mathbf{n} \mathbf{B} = \mathbf{T}, \quad (17)$$

where  $\mathbf{n}$  is a matrix of weights and  $\mathbf{T}$  is a matrix containing the target spatial harmonic basis functions as its rows, as depicted in Fig. 4(c). The least squares solution

$$\mathbf{n} = \mathbf{T} \mathbf{B}_{\text{pseudo}}^{-1} \quad (18)$$



is just the product of the matrix of target basis functions with the Moore–Penrose pseudoinverse of the encoding matrix. Subsequent Fourier transformation [Fig. 4(c)] then corresponds to multiplication by  $\mathbf{T}^{-1}$ . When the pseudoinverse of  $\mathbf{B}$  is restricted to the minimal subblock, the calculation of  $\mathbf{n}$  reduces to the familiar SMASH spatial harmonic fitting procedure.<sup>10</sup>

The Moore–Penrose pseudoinverse is known to produce the minimum-length solution to least squares fitting problems.<sup>27,29</sup> In fact, as a result of this property, it will in principle yield the highest possible SNR in reconstructed images. SNR in parallel MR image reconstructions has been shown to depend upon the magnitudes of the weight factors used in the reconstruction.<sup>11,30</sup> The Moore–Penrose pseudoinverse minimizes the length (i.e., the summed absolute magnitude) of the vector of weights used to generate each pixel in the reconstructed image, and therefore minimizes the degree of noise amplification for any given pixel intensity. Indeed, the SNR-optimized “weak” reconstruction derived in Ref. 11 is just the Moore–Penrose pseudoinverse of the encoding matrix, adjusted to compensate for the effects of existing noise correlations through the inclusion of a noise resistance matrix  $\mathbf{R}$ :<sup>11,28</sup>

$$\mathbf{B}_{\text{pseudo, noise-adjusted}}^{-1} = (\mathbf{B}^\dagger \mathbf{\Psi}^{-1} \mathbf{B})^{-1} \mathbf{B}^\dagger \mathbf{\Psi}^{-1}. \quad (19)$$

For a fully gradient-encoded acquisition, this formula naturally reduces to the matched filter component coil combination procedure which has been shown to optimize SNR in phased-array imaging.<sup>28</sup>

SNR degradations in parallel MR image reconstructions will clearly occur whenever the elements of the inverted encoding matrix are large. The size of the inverse, in turn, is related to the degree of linear independence of the encoding functions which make up the encoding matrix. For example, when the sensitivities of any two component coils overlap too severely, different rows of the encoding matrix become nearly identical. This degeneracy causes the encoding matrix to become nearly singular, and therefore highly susceptible to noise amplification as well as to random or systematic errors in the calibration of sensitivities and the determination of the encoding matrix elements. More concretely, degenerate encoding functions result in small eigenvalues for the encoding matrix, and these small eigenvalues produce large weight factors, thereby degrading SNR.

From this perspective, the numerical conditioning inherent in SMASH or an expanded subblock hybrid approach may be understood as the result of alleviating potential singularities in the encoding matrix by decreasing its effective dimensionality and increasing the degree of overdetermination of the fitting problem. In addition to the numerical conditioning provided by subblock diagonalization, further numerical conditioning may also be added directly to the  $\mathbf{B}$  matrix inversion. Here, we proceed along lines suggested by the model of numerical conditioning currently used in SMASH reconstructions.<sup>10</sup>

It is clear that the smallest eigenvalues of  $\mathbf{B}^\dagger \mathbf{B}$  in Eq. (14), or the smallest diagonal elements of  $\mathbf{D}$  in Eq. (15), represent potential numerical instabilities in the reconstruction. Since

small eigenvalues will be inverted to large values in the inverse, either noise or systematic errors in sensitivity calibration affecting the eigenvectors associated with these small eigenvalues will be amplified in the reconstruction. One possible approach to preventing such amplification involves establishing a minimum eigenvalue threshold and performing one of the following procedures:

- (1) eliminating all eigenvalues below the threshold from the inversion,
- (2) setting all subthreshold eigenvalues equal to the threshold value, or
- (3) adding the threshold value to all eigenvalues.

The numerical conditioning approach described for SMASH reconstructions in Ref. 10 corresponds to application of the third procedure in the list above to the spatial harmonic fit (which we may now identify as the Moore–Penrose pseudoinverse of a subblock of the full encoding matrix). By definition, any of the procedures listed above will improve the condition number of the encoding matrix, defined as the ratio of the maximum to the minimum eigenvalue. More advanced conditioning strategies may also be adopted at will from the extensive literature on linear algebra. In any case, the result of the numerical conditioning process is to modify or eliminate from the inversion the components most responsible for noise and error propagation, resulting in improved SNR and reduced artifact in the reconstructed images.

The price of these improvements is the omission of certain features of the reconstructed image in regions most susceptible to numerical instability. To the extent that these features are genuine components of the image, their omission will result in artifacts. On the other hand, conditioning will control or eliminate the most severe artifacts associated with errors in sensitivity calibration. By artificially limiting the magnitude of the encoding matrix inverse, conditioning also allows increases in image SNR beyond what may be possible even using perfectly calibrated sensitivities, and this may be the most important determinant of overall image quality, lesion conspicuity, etc., in images with a low inherent SNR. In short, numerical conditioning allows a tunable tradeoff between idealized accuracy and practical image quality and SNR.

Figure 9 demonstrates the effects of numerical conditioning in a sixfold accelerated phantom image reconstruction, using the same source data as was used in Fig. 7. Figure 9(a) shows the results of the same full encoding matrix inversion as was used in Fig. 7(c), highlighting once again the numerical instabilities resulting from high acceleration and large oblique angulation of the image plane with respect to the coil array. In Fig. 9(b), all singular values of the full encoding matrix falling below a threshold value of 10% of the maximum singular value were set equal to the threshold in the SVD prior to inversion. The resulting image has been largely cleared of pointwise artifacts, revealing the underlying structure of the phantom. Any artifacts resulting from this eigenvalue conditioning procedure fall beneath the residual noise floor of the image and are not visible in the figure. For com-



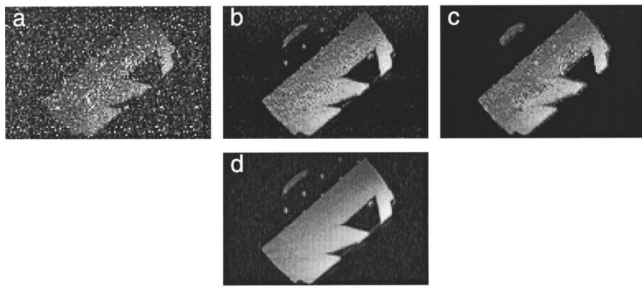


FIG. 9. (a)–(c) Sixfold accelerated double-oblique images of a phantom reconstructed from the same acquired data as was used in Fig. 7. (a) Unconditioned image-domain reconstruction using raw component coil images as sensitivity references, without body coil reference and without sensitivity postprocessing. (b) Conditioned image-domain reconstruction using raw component coil sensitivity references and a relative SVD threshold of 10%. All singular values falling below a threshold of 10% of the maximum singular value were set equal to the threshold value in the SVD of the encoding matrix prior to inversion. (c) Unconditioned SENSE reconstruction using postprocessed sensitivity references. Component coil sensitivity reference images were divided by a separately acquired body coil reference image and subjected to the several-stage postprocessing algorithm described in Ref. 11 to generate sensitivity maps. (d) Unaccelerated reference image formed as the square root of the sum of squares of fully gradient-encoded component coil images.

parison, Fig. 9(c) shows the results of a full unconditioned inversion using the sensitivity postprocessing algorithm described in Ref. 11 and Fig. 9(d) shows an unaccelerated sum of squares reference combination of fully gradient-encoded component coil images.

Eigenvalue conditioning may be applied to encoding matrix inversions in the image-domain pixel basis, the  $k$ -space Fourier basis, or any other mixed basis, either for a full inverse or for an isolated subblock approach. The effect of conditioning will also vary somewhat depending upon the structure of the particular matrix to be inverted. For example, the results of conditioning a full generalized encoding matrix inverse will differ from the results of separately conditioned pixel-by-pixel image-domain inversions. Specifically, in the generalized  $\mathbf{B}$  matrix inversion, eigenvalue thresholds may be applied to entire matrices, or to matrix blocks governing the reconstruction of multiple different pixels. Thus, particular image regions may be eliminated or approximated based on a comparison with neighboring regions, rather than by application of a single region-independent criterion.

### E. Coil sensitivity calibration

In order for a parallel MR image reconstruction to proceed, the entries of the encoding matrix must first be filled with accurate representations of the actual coil sensitivities and gradient modulations entering into the acquired MR signal. The choice of encoding matrix inversion strategy has implications for both the quantity and the character of sensitivity calibration information required.

Strategies such as subencoding or SENSE have generally required accurate estimates of sensitivities for each pixel position in the reconstructed image. SMASH image reconstructions, by contrast, have been shown to require as little as a single  $k$ -space line for calibration using the AUTO-SMASH

technique.<sup>13</sup> This flexibility in calibration may be traced once again to the repeating block structure of the encoding matrix. To the extent that the  $\mathbf{B}$  matrix may be reliably inverted block by block, sensitivity calibration for a single block will suffice to generate the full inverse. As the size of the inverted subblock is increased, for example in the hybrid reconstructions introduced earlier in this article, the amount of calibration information required to invert each block will also increase.

*In vivo* sensitivity estimates are commonly used for many of the parallel imaging techniques. In the SENSE approach, carefully postprocessed quotients of *in vivo* reference images are used as sensitivity maps.<sup>11</sup> The use of raw *in vivo* references without postprocessing has recently been reported for SMASH applications, taking advantage of degrees of freedom in the spatial harmonic fitting procedure.<sup>10</sup> An image domain technique using uncorrected *in vivo* reference images has also been described.<sup>7</sup> These latter approaches may easily be generalized to arbitrary encoding matrices, and, in combination with numerical conditioning, may be used to eliminate most of the stringent requirements for sensitivity postprocessing in practical applications.

To a good approximation, an *in vivo* reference image obtained with any component coil  $l$  is simply the sensitivity  $C_l$  of that coil multiplied by a function  $\sigma$  reflecting the underlying spin density as well as any relaxation or other sequence-specific effects associated with the reference acquisition:

$$I_l^{\text{reference}}(x, y) = C_l(x, y) \sigma(x, y). \quad (20)$$

The  $\sigma$  function will generally differ significantly from the target spin density  $\rho$ , since the imaging sequence used for reference image acquisition will generally have a different spatial resolution, temporal resolution, and contrast than the sequence used for parallel MR image acquisition. Typically, rapidly-acquired low-resolution images are used as sensitivity references. In the approach described in Ref. 11, component coil reference images  $I_l^{\text{reference}}$  are divided by a separately acquired body coil image representative of  $\sigma$  alone (or else by a suitable combination image), and several stages of smoothing and filtering are applied in order to regularize the resulting estimate of  $C_l$ . (A related approach has been described which also uses ratios of reference images.<sup>21</sup>) Though this approach has been shown to yield accurate sensitivity estimates in many cases, the additional body coil acquisition and the added postprocessing time can be cumbersome, and special care must also be taken to avoid calibration errors, since the quotient image may be poorly behaved especially in regions of low SNR.

Since the  $\sigma$  function is shared between all component coils, however, it does not inherently affect the independence of spatial information in the encoding matrix, and it may be made to divide out of the reconstruction itself, without ever requiring computation of an explicit quotient image. In particular, if the sensitivities  $C_l$  are replaced by *in vivo* reference images  $I_l^{\text{reference}} = C_l \sigma$ , the elements of the encoding matrix and its inverse become

$$B_{(k_x, k_y, l), (x, y)} \rightarrow B_{(k_x, k_y, l), (x, y)} \sigma_{(x, y)}, \quad (21)$$

$$B_{(x, y), (k_x, k_y, l)}^{-1} \rightarrow \sigma_{(x, y)}^{-1} B_{(x, y), (k_x, k_y, l)}^{-1}.$$

Equation (8) relating the measured signal to the reconstructed image intensity then undergoes the following simple modification:

$$\rho = \mathbf{B}^{-1} \mathbf{S} \rightarrow \sigma^{-1} \rho = (\sigma^{-1} \mathbf{B}^{-1}) \mathbf{S}, \quad (22)$$

where  $\sigma^{-1}$  is a diagonal matrix containing the reciprocals  $\sigma_{(x, y)}^{-1}$  along the diagonal. In other words, the image reconstructed by inversion of an encoding matrix constructed from uncorrected *in vivo* reference images is just the pixelwise quotient of the true image intensity with the reference density function  $\sigma$ . The final image may be corrected for  $\sigma$  through postmultiplication by any appropriate combination of reference images, each of which itself contains  $\sigma$ . For example, postmultiplication by a sum-of-squares combination of reference images yields the desired spin density multiplied by the sum of squares of component coil sensitivities:

$$\left( \sum_l |\mathbf{I}_l^{\text{reference}}|^2 \right)^{1/2} (\sigma^{-1} \mathbf{B}^{-1}) \mathbf{S} = \left( \sum_l |\mathbf{C}_l|^2 \right)^{1/2} \sigma \sigma^{-1} \rho$$

$$= \left( \sum_l |\mathbf{C}_l|^2 \right)^{1/2} \rho. \quad (23)$$

The reconstructed image described by Eq. (23) does not differ in principle from the image which would have resulted from dividing all component coil reference images by their sum of squares combination prior to formation of the encoding matrix. In other words, to this point, we have only succeeded in moving the quotient from one side of the reconstruction to the other. The benefits of this transformation result from a favorable interaction with the numerical conditioning procedures already discussed.

Appropriate regularization of the sensitivity reference quotient in the SENSE approach requires application of a thresholding procedure which eliminates all regions falling below an established intensity and/or density threshold in the denominator.<sup>11</sup> However, the unstable regions of the quotient image generally correspond to unstable regions in the encoding matrix inversion (i.e., regions associated with small eigenvalues). Thus, the use of eigenvalue conditioning will result in *automatic* thresholding. All regions destined to yield large errors in the reconstruction, including those which result from unstable low-SNR regions in the reference images, are removed or regularized in a single step. As a result, eigenvalue conditioning may be used conveniently in conjunction with simple *in vivo* sensitivity references, without additional correction or thresholding and without requiring acquisition of an accompanying body coil image.

In addition to its function in controlling SNR degradation, then, numerical conditioning also serves to reduce the degree of processing to which raw sensitivity measurements must be subjected in practical parallel image reconstructions. The regularizing effect of eigenvalue conditioning may be appreciated in Fig. 9(b). This image, along with the image in Fig. 9(a), was generated using raw component coil sensitivity ref-

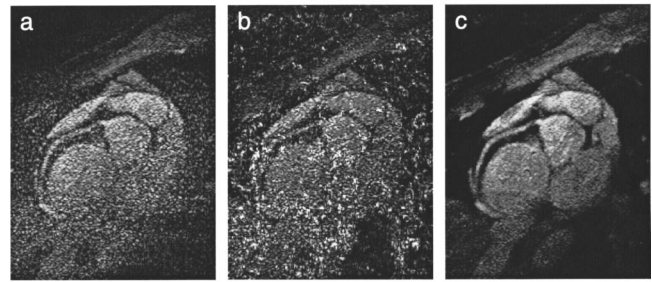


FIG. 10. Fivefold accelerated double-oblique cardiac MR images obtained using a six-element array. (a) SMASH reconstruction. (b) Unconditioned image domain reconstruction. (c) Conditioned image-domain reconstruction using a relative SVD threshold of 25% of the maximum singular value. Image data were acquired in a healthy adult subject using a navigator gated and corrected  $T_2$  prepared 3D TFE imaging sequence<sup>33,34</sup> (TR=8.8 ms, TE=2.4 ms, matrix size=76×512 reconstructed to 380×512, in-plane spatial resolution 0.7×1.0 mm<sup>2</sup>, 10 slices interpolated to 20, through plane resolution 3 mm interpolated to 1.5 mm, acquisition window 70 ms per cardiac cycle) on a Philips NT 1.5T imaging system (Philips Medical Systems, Best, The Netherlands). A single image slice from the 3D double-oblique acquisition is shown, displaying an extended segment of the right coronary artery. Low-resolution *in vivo* component coil images acquired separately with the same sequence were used as sensitivity references in all cases, without a body coil reference and without sensitivity postprocessing.

erences acquired with a separate acquisition in the same phantom. No body coil reference was used, and no postprocessing was applied other than the postmultiplication step of Eq. (23). The image in Fig. 9(c), on the other hand, was generated without conditioning using the full postprocessing procedure described in Ref. 11: component coil sensitivity references containing the phantom spin density were divided by a body coil reference from a third acquisition, and thresholding, filtering, and smoothing were applied as outlined in Ref. 11. As expected, sensitivity postprocessing does eliminate artifacts resulting from regions of inadequately characterized sensitivity. Our particular implementation, which used parameters optimized separately for *in vivo* reconstructions, also removes several isolated phantom features such as the line of bright dots running diagonally upward from left to center. Though postprocessing parameters could certainly be chosen to retain these features, they are automatically retained by the eigenvalue conditioning approach, which uses the specific criterion of numerical stability rather than other image-based criteria as the basis for constraining the reconstruction.

### III. IN VIVO RESULTS

Figure 10 compares reconstructions of a fivefold accelerated cardiac MR image using an unconditioned SMASH reconstruction, an unconditioned image domain reconstruction, and an image domain reconstruction with eigenvalue conditioning, respectively. These reconstructions were performed on the same data set obtained in a healthy adult subject with a six-element array<sup>31,32</sup> using a 3D  $T_2$ -prepared navigator gated and corrected turbo field echo imaging sequence<sup>33,34</sup> on a Philips NT scanner (Philips Medical Systems, Best, The Netherlands). In all cases, an *in vivo* sensitivity reference was used, without body coil reference or sensitivity postpro-

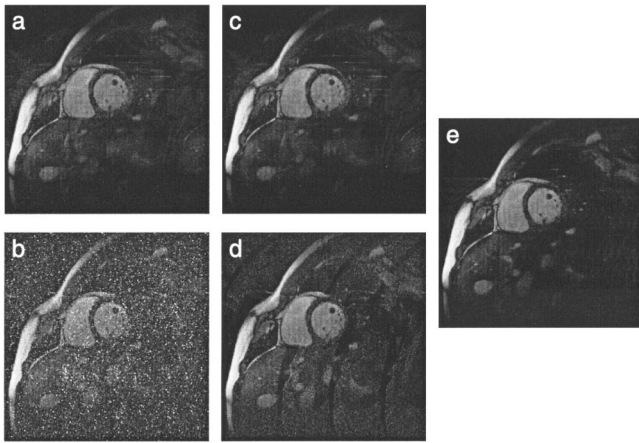


FIG. 11. Fourfold accelerated short-axis cardiac MR images using a four-element array. (a) Unconditioned SMASH reconstruction. (b) Unconditioned image domain reconstruction. (c) Conditioned SMASH reconstruction (10% relative SVD threshold). (d) Conditioned image domain reconstruction (10% relative SVD threshold). (e) Conditioned expanded-subblock hybrid reconstruction (subblock size = 7 times minimum block size, 10% relative SVD threshold). Image data were acquired in a healthy adult subject using a TrueFISP cine imaging sequence (TR = 3.5 ms, TE = 1.8 ms, matrix size =  $64 \times 256$  reconstructed to  $256 \times 256$ , FOV =  $87.5 \times 350$  mm<sup>2</sup> reconstructed to  $350 \times 350$  mm<sup>2</sup>, slice thickness = 6 mm, 15 lines per cine segment) on a Siemens Symphony 1.5T scanner with Quantum gradients (Siemens Medical Systems, Erlangen, Germany). A single frame of the gated cine acquisition is shown. *In vivo* component coil images acquired separately with the same imaging sequence were used as sensitivity references in all cases, without a body coil reference and without sensitivity postprocessing.

cessing. SMASH reconstruction was performed using the tailored spatial harmonic fitting procedures outlined in Ref. 10. Image domain reconstructions were performed using pixel-by-pixel inversions as in Eq. (13) followed by the postmultiplication step of Eq. (23). For numerical conditioning in Fig. 10(c), a threshold value of 25% of the maximum singular value in the SVD was chosen, with subthreshold elements set equal to the threshold value prior to inversion.

Both the SMASH reconstruction in Fig. 10(a) and the conditioned reconstruction in Fig. 10(c) control the pointwise artifacts which contaminate the unconditioned image in Fig. 10(b). However, the numerical conditioning in Fig. 10(c) results in superior SNR, and includes automatic regularization of *in vivo* regions such as the lungs in which sensitivities are poorly characterized. As a result, the course of the right coronary artery may be clearly discerned in Fig. 10(c). Note that the five-fold acceleration shown here approaches the theoretical maximum achievable factor for a six-element array. Even at this high acceleration, and for a particularly challenging double-oblique image plane, no aliasing artifacts are visible, and numerical conditioning preserves high image quality.

Figure 11 compares various image reconstruction strategies with and without numerical conditioning for a fourfold accelerated short-axis cardiac image obtained with a four-element array. A TrueFISP cine imaging sequence was used for data acquisition on a Siemens Symphony 1.5T scanner with Quantum gradients (Siemens Medical Systems, Erlangen, Germany), with the flexible linear array contoured to the

chest wall of a healthy adult subject. Once again, raw *in vivo* component coil sensitivity reference images from a separate acquisition were used, without body coil reference or sensitivity postprocessing. SMASH reconstructions were performed as in Ref. 10, and image domain reconstructions were performed as in Eqs. (13) and (23).

The unconditioned SMASH image in Fig. 11(a) shows evidence of mild residual aliasing, whereas the unconditioned image domain reconstruction in Fig. 11(b) contains pointwise instabilities. Eigenvalue conditioning of the minimum-subblock SMASH reconstruction using an SVD threshold of 10% of the maximum singular value has little additional effect on image quality [Fig. 11(c)]. Conditioning of the fully inverted image domain reconstruction using the same relative SVD threshold of 10% controls most of the pointwise instabilities, but leaves some aliased residual [Fig. 11(d)]. The best image quality is obtained using a combination of generalized hybrid reconstruction with numerical conditioning (subblock size = 7 times minimum block size, SVD threshold = 10% of maximum). Residual aliasing artifacts are slight, and no pointwise artifacts are in evidence. The result is a high-quality image at the maximal acceleration factor of 4 for this four-element array, even in a highly angulated cardiac short-axis plane.

## IV. DISCUSSION

### A. Additional dimensions and generalizations

For most of the illustrations in this article, the case of two-dimensional imaging with a single phase encoding direction was used for simplicity and clarity of presentation. With the insertion of additional spatial indices as needed to the integral representation of the MR signal, generalization of the theory presented here to the case of multiple phase-encoded/coil-encoded directions is straightforward. Of course, such situations may require inversion of larger subsets of the full **B** matrix, at some cost in processing time.

Even though the majority of existing parallel imaging techniques may be associated with either the pixel basis or the Fourier basis as illustrated in Fig. 4, alternative target bases may also be used to advantage. For example, if direct inversion of the **B** matrix to a spatially localized delta function basis is poorly behaved, a partially localized set of basis functions, such as wavelets, Gaussians, or sinc functions, may be used as an intermediate. Final transformation to the pixel basis may then be accomplished using a procedure such as deconvolution, which may be apodized or otherwise modified to control instabilities which would result from direct inversion.<sup>35</sup>

It was mentioned in the initial derivation of the encoding matrix that the discretizing assumption leading to Eq. (4) does not significantly compromise the generality of the results. In order to support this claim, the general case of continuous encoding functions is explored in the Appendix, and the implications of various strategies of discretization are discussed.

It is shown in the Appendix that a parallel image reconstruction, or an MR image reconstruction in general, may be



viewed as a linear fitting of the continuous encoding functions in Eq. (2) to target voxel shape functions at each voxel position. Various possible definitions of discrete encoding functions are then shown simply to represent alternative choices of generalized fitting procedures. A similar fitting approach was used in Ref. 11 to derive “strong” and “weak” parallel reconstruction algorithms. Application of the matrix formulation of the current article to the generalized fitting problem, however, validates the use of tools such as sub-block inversion and numerical conditioning in the most general case. Using the generalized formulation of the Appendix, it becomes clear that the encoding properties of RF coils and gradients may even be exploited to vary target voxel shapes across an image, which may be of use for applications with rigorous demands on spatial resolution, SNR, and voxel isolation.

### B. $k$ -space sampling trajectories

The case of regular Cartesian  $k$ -space sampling is still most frequently used in practical imaging applications. The typical parallel MR image acquisition then involves omission of regularly spaced intermediate  $k$ -space lines, and subsequent “unfolding” to full FOV of the resulting aliased data sets. However, as long as the total number of acquired data points in all array elements is greater than or equal to the number of voxels in the image to be reconstructed, there is an “exact” solution to the parallel image reconstruction (assuming sensitivities are known exactly). Thus, any arbitrary  $k$ -space sampling trajectory may in principle be accommodated.

For example, in contrast to the typical parallel MR acquisition, component coil MR signal data may be acquired only in the center of  $k$ -space and may be used to reconstruct signals at the edges of  $k$ -space. In other words, image data at low resolution and full FOV may be acquired and reconstructed directly to high resolution. The price for such an approach will lie in the magnitude of the weights required for reconstruction. Large weights will result in a high degree of noise multiplication and a low SNR unless stringent numerical conditioning is employed.

As another example, spiral  $k$ -space trajectories are also amenable to parallel reconstruction, and spiral imaging with SENSE has been described.<sup>36</sup> The size of the encoding matrices for spiral acquisitions has raised serious computational issues, and algorithmic improvements have been called for to reduce reconstruction times.<sup>37,38</sup> The inversion of encoding matrix subblocks of reduced dimensionality would significantly simplify the processing required, but suitable subblocks have yet to be identified for the spiral case.

Even for the case of sampling on a Cartesian grid, it has been proposed that variable  $k$ -space sampling densities may be exploited to improve parallel image reconstructions.<sup>22,25</sup> In an extension of these approaches, the generalized formalism outlined here could be used to tailor acquisitions directly to the parallel reconstruction. For example, the SVD of typical Cartesian encoding matrices could be used to design non-Fourier sampling strategies in which image components as-

sociated with principal components of the encoding matrix itself are acquired directly. Such an approach would guarantee acquisition of precisely the image components which are most compatible with spatial encoding by coil arrays. Rather than being retrospectively removed through an eigenvalue threshold as in the conditioning approaches described here, image components which are destined to produce noise and error would be prospectively eliminated from the acquisition in this approach, thereby making even more efficient use of precious acquisition time.

### C. Implications for coil array design

It should also be noted that insights derived from the generalized approach outlined here may be used to guide the design of coil arrays for parallel imaging. The inherent degree of independence of subblocks in a measured  $\mathbf{B}$  matrix may be used to assess the encoding capabilities of any given array, and to select among various candidate designs. Arrays may also be designed to produce sensitivities close to a basis of choice, and therefore to allow inherently well-conditioned encoding matrix inversions and parallel image reconstructions.

## V. CONCLUSIONS

The formalism presented in this article demonstrates that the various parallel MR imaging techniques that have been proposed to date share a common starting point, with encoding functions grouped into a suitably defined encoding matrix. The most common implementations of techniques such as SMASH and SENSE may be derived by application of various basis transformations or fitting procedures to the generalized encoding matrix. The particular properties of each technique may then be tied to its particular choice of encoding matrix inversion strategy.

Clearly, the parallel imaging process does not end once entries of the encoding matrix are determined. Investigation of the physical structure of encoding matrices, and attention to the details of matrix inversion, not only elucidates the relation between techniques, but also suggests new reconstruction algorithms with improved performance. Idealized accuracy may be traded off against practical robustness and computational convenience through the use of suitable approximations or regularization procedures, such as numerical conditioning or hybrid subblock inversion. Numerical conditioning of encoding matrix inversion enables effective compensation for noise or for systematic errors in coil sensitivity calibration, and can result in improved image quality and SNR under a wide range of conditions, even or especially at the extremes of performance of parallel MRI techniques. Hybrid approaches, in combination with numerical conditioning, also extend the useful range of parallel imaging techniques, and allow robust parallel image reconstructions at high accelerations.

## ACKNOWLEDGMENTS

The authors would like to acknowledge Dr. Matthias Stuber and Dr. Rene Botnar for developing and making avail-

able to us the imaging sequence used to acquire the coronary MR images in Fig. 10. Partial support for this work was provided by the National Institutes of Health (NIH R29 HL60802), and by the Whitaker Foundation's Biomedical Engineering Grant program.

## APPENDIX: CONTINUOUS ENCODING FUNCTIONS AND DISCRETIZATIONS

The measured MR signals as expressed in Eq. (1) are truly integrated signals: they are projections of functions  $B$  and  $\rho$  whose spatial variations are in actuality continuous down to the atomic level. The reconstructed MR image, on the other hand, constitutes a discrete representation of the spin density  $\rho$  (appropriately convolved by relaxation effects) at a finite set of voxel positions with far greater than atomic spacing. Clearly each reconstructed voxel value must itself represent some integration of the continuous spin density over the volume represented by the voxel.

If we choose a target voxel shape, the most general case of MR image reconstruction may then be expressed as a fit of the continuous encoding functions to this continuous voxel shape, which defines the region over which the continuous spin density must be integrated to yield the reconstructed voxel value. Given a target voxel shape function  $V(\bar{x}, \bar{y}, x, y)$  centered at the discrete spatial position  $(\bar{x}, \bar{y})$ , we wish to find the linear combination of encoding functions which yields the closest approximation to that shape:

$$V(\bar{x}, \bar{y}, x, y) \approx \sum_{k_x, k_y, l} n_{(\bar{x}, \bar{y}), (k_x, k_y, l)} B_l(x, y, k_x, k_y). \quad (\text{A1})$$

In matrix form, Eq. (A1) becomes

$$\mathbf{V}_c \approx \mathbf{n} \mathbf{B}_c. \quad (\text{A2})$$

The  $c$  subscript labeling the  $\mathbf{V}_c$  and  $\mathbf{B}_c$  matrices in Eq. (A2) indicates that these matrices are made up of *continuous* functions (the voxel shape functions or the encoding functions, respectively), and therefore have infinite dimension with respect to the continuous spatial indices ( $x$  and  $y$ ). Standard matrix multiplication conventions continue to apply, as long as all inner products involving sums over the continuous indices are replaced with integrals.  $\mathbf{B}_c$  may also be understood as a continuous analog to the discrete encoding matrix  $\mathbf{B}$ .  $\mathbf{B}_c$  has the same structure as the encoding matrices shown in Figs. 3–6, simply with continuous functions along each of its rows.

The best least-squares solution of the fitting problem in Eq. (A2) is

$$\mathbf{n}^{\text{least squares}} = \mathbf{V}_c \mathbf{B}_c^\dagger (\mathbf{B}_c \mathbf{B}_c^\dagger)^{-1}. \quad (\text{A3})$$

One may recognize the formula for the Moore–Penrose pseudoinverse in Eq. (A3), indicating that each row of  $\mathbf{n}^{\text{least squares}}$  is the minimum-length vector which solves the least squares fitting problem. Although the matrices  $\mathbf{B}_c$  and  $\mathbf{V}_c$  have one infinite dimension each [ $\dim(\mathbf{B}_c) = N_x^* N_y^* L/M \times \text{Inf}$  and  $\dim(\mathbf{V}_c) = N_x^* N_y \times \text{Inf}$ ], the products  $\mathbf{B}_c \mathbf{B}_c^\dagger$  and  $\mathbf{V}_c \mathbf{B}_c^\dagger$  in Eq. (A3) are finite-dimensional, due to integration over the continuous dimension [ $\dim(\mathbf{B}_c \mathbf{B}_c^\dagger) = N_x^* N_y^* L/M$

$\times N_x^* N_y L/M$  and  $\dim(\mathbf{V}_c \mathbf{B}_c^\dagger) = N_x^* N_y \times N_x^* N_y^* L/M$ ]. Replacing internal sums over continuous variables  $x$  and  $y$  with corresponding integrals, we may express the elements of the finite-dimensional matrices  $\mathbf{B}_c \mathbf{B}_c^\dagger$  and  $\mathbf{V}_c \mathbf{B}_c^\dagger$  as follows:

$$\begin{aligned} (\mathbf{B}_c \mathbf{B}_c^\dagger)_{(k'_x, k'_y, l'), (k_x, k_y, l)} &= \sum_{x, y} B_{c(k'_x, k'_y, l'), (x, y)} B_{c(x, y), (k_x, k_y, l)}^\dagger \\ &\rightarrow \int dx dy B_{l'}(x, y, k'_x, k'_y) B_l^\dagger(x, y, k_x, k_y), \end{aligned} \quad (\text{A4})$$

$$\begin{aligned} (\mathbf{V}_c \mathbf{B}_c^\dagger)_{(\bar{x}, \bar{y}), (k'_x, k'_y, l')} &= \sum_{x, y} V_{c(\bar{x}, \bar{y}), (x, y)} B_{c(x, y), (k'_x, k'_y, l')}^\dagger \\ &\rightarrow \int dx dy V(\bar{x}, \bar{y}, x, y) B_{l'}^\dagger(x, y, k'_x, k'_y). \end{aligned} \quad (\text{A5})$$

With these definitions,  $\mathbf{n}^{\text{least squares}}$  in Eq. (A3) is identical to the “strong” case reconstruction matrix derived in Ref. 11.

Weighting of the measured MR signals by the weights  $\mathbf{n}^{\text{least squares}}$  yields an estimate of spin density at the chosen voxel position  $(\bar{x}, \bar{y})$ :

$$\begin{aligned} \sum_{k_x, k_y, l} n_{(\bar{x}, \bar{y}), (k_x, k_y, l)}^{\text{least squares}} S_l(k_x, k_y) &= \int dx dy \sum_{k_x, k_y, l} n_{(\bar{x}, \bar{y}), (k_x, k_y, l)}^{\text{least squares}} B_l(x, y, k_x, k_y) \rho(x, y) \\ &\approx \int dx dy V(\bar{x}, \bar{y}, x, y) \rho(x, y) \\ &\equiv \bar{\rho}(\bar{x}, \bar{y}). \end{aligned} \quad (\text{A6})$$

The spin density estimate  $\bar{\rho}(\bar{x}, \bar{y})$  in Eq. (A6) is just the continuous spin density  $\rho(x, y)$  integrated over a volume defined by the least-squares approximation to the localized voxel function  $V(\bar{x}, \bar{y}, x, y)$ . In the case for which the same target voxel shape is used at all positions in the reconstructed image, we may write  $V(\bar{x}, \bar{y}, x, y) \rightarrow V(x - \bar{x}, y - \bar{y})$ , and Eq. (A6) represents a convolution of the spin density against the best-fit voxel shape. The fitting of encoding functions to voxel shapes then resembles Green's function analysis in electromagnetic theory or in other well-known physical theories for which the superposition principle applies. First, the “unit” case is solved, then the results are convolved against the particular distribution of interest to yield the desired result.

Equation (A6) also bears a marked resemblance to the basic equations for SMASH image reconstruction, and in fact the most general parallel reconstruction may be viewed as a generalization of the SMASH fitting procedure. In SMASH, we use the condition that

$$\sum_l n_l^{(m)} C_l(x, y) \approx C_0(x, y) \exp(im \Delta k_y y) \quad (\text{A7})$$

to produce shifted composite signals

$$\begin{aligned}
\sum_l n_l^{(m)} S_l(k_x, k_y) &= \int dx dy \sum_l n_l^{(m)} C_l(x, y) \\
&\quad \times \exp(-ik_x x) \exp(-ik_y y) \rho(x, y) \\
&\approx \int dx dy C_0(x, y) \exp(-ik_x x) \\
&\quad \times \exp(-i(k_y - m\Delta k_y)y) \rho(x, y) \\
&\equiv S(k_x, k_y - m\Delta k_y). \quad (A8)
\end{aligned}$$

Just as weighting of component coil signals at one given  $k$ -space index in SMASH propagates across the integral in Eq. (A8) to produce composite spatial harmonic modulations and shifted signals, so the weighting of measured signals at all  $k$ -space indices propagates across the integral in Eq. (A6) to yield an estimate of spin density at each position in the image domain. The results of the analysis for continuous encoding functions thus bears out the conclusions already derived for the discrete case: the SMASH fit is just a select subset of the full generalized fit, with the Fourier transform separated out as a distinct step.

The weight matrix  $\mathbf{n}^{\text{least squares}}$  in Eq. (A3) may be understood more generally as an analog of the  $\mathbf{B}$  matrix inverse for the case of continuous encoding functions. For the continuous case,

$$\rho \approx \mathbf{n}^{\text{least squares}} \mathbf{S} = (\mathbf{V}_c \mathbf{B}_c^\dagger (\mathbf{B}_c \mathbf{B}_c^\dagger)^{-1}) \mathbf{S}, \quad (A9)$$

whereas in the discrete representation used elsewhere in this article,

$$\rho \approx \mathbf{B}_{\text{pseudo}}^{-1} \mathbf{S} = ((\mathbf{B}^\dagger \mathbf{B})^{-1} \mathbf{B}^\dagger) \mathbf{S} \quad (A10)$$

(assuming a unit noise resistance matrix  $\mathbf{R}=\mathbf{1}$ ). As is indicated in Eq. (A5), multiplication by  $\mathbf{V}_c$  is equivalent to integration against the localized voxel functions  $V(\bar{x}, \bar{y}, x, y)$ ; thus, the voxel shape matrix  $\mathbf{V}_c$  serves as a discretization operator against which the pseudoinverse of the continuous encoding matrix is multiplied to generate a discrete set of best-fit weight factors.

A finite-dimensional  $\mathbf{B}$  matrix may be also generated directly from the continuous encoding matrix  $\mathbf{B}_c$  through multiplication by  $\mathbf{V}_c$ :

$$\mathbf{B} = \mathbf{V}_c \mathbf{B}_c^\dagger. \quad (A11)$$

This definition of the encoding matrix corresponds to the “weak” reconstruction formalism defined in Ref. 11. It results in a different set of weights, and hence in different actual voxel shapes and SNR profile, than the true least squares solution of Eq. (A3).

The formation of discrete encoding matrices prior to inversion has certain practical advantages. First of all, since coil sensitivity estimates are derived in practice from *in vitro* or *in vivo* MR images which are themselves discrete estimates of continuously varying functions, discrete encoding matrix elements are more practical to compute than the idealized overlap integrals of continuous encoding functions in Eq. (A4). Under the condition of Eq. (A11), different discretization procedures correspond simply to the choice of

different target voxel shape functions. If delta-function voxel shapes are chosen, the encoding matrix elements in Eq. (A11) are just the continuous functions evaluated at the center of each pixel. A choice of rectangular voxel shapes gives encoding matrix elements which are averages of the continuous functions over each voxel volume.

The definition of a discrete encoding matrix as in Eq. (A11), rather than just a discrete least-squares solution as in Eq. (A3), also facilitates the algebraic analysis leading to hybrid reconstructions and practical numerical conditioning approaches. Nevertheless, the formalism presented in this Appendix shows that hybrid reconstructions and numerical conditioning may also be defined, if desired, for the case of continuous encoding functions, through least-squares fitting of selected subblocks of the continuous encoding matrix  $\mathbf{B}_c$ , or through modification of the eigenvalues of the finite-dimensional matrix  $\mathbf{B}_c \mathbf{B}_c^\dagger$  in Eq. (A3).

<sup>a)</sup>Address for correspondence: Cardiovascular Division, Beth Israel Deaconess Medical Center, 1 Autumn Street, Fifth Floor, Room AK-512, Boston, MA 02215. Electronic mail: dsodicks@caregroup.harvard.edu

<sup>1</sup>D. K. Sodickson, “Spatial encoding using multiple RF coils: SMASH imaging and parallel MRI,” in *Methods in Biomedical Magnetic Resonance Imaging and Spectroscopy*, edited by I. R. Young (Wiley, Chichester, 2000), pp. 239–250.

<sup>2</sup>J. W. Carlson, “An algorithm for NMR imaging reconstruction based on multiple RF receiver coils,” *J. Magn. Reson.* **74**, 376–380 (1987).

<sup>3</sup>M. Hutchinson and U. Raff, “Fast MRI data acquisition using multiple detectors,” *Magn. Reson. Med.* **6**(1), 87–91 (1988).

<sup>4</sup>J. R. Kelton, R. L. Magin, and S. M. Wright, “An algorithm for rapid image acquisition using multiple receiver coils,” in *Proceedings of the Eighth Annual Meeting of the Society for Magnetic Resonance in Medicine*, Amsterdam, Netherlands (1989), p. 1172.

<sup>5</sup>D. Kwiat, S. Einav, and G. Navon, “A decoupled coil detector array for fast image acquisition in magnetic resonance imaging,” *Med. Phys.* **18**(2), 251–265 (1991).

<sup>6</sup>J. W. Carlson and T. Minemura, “Imaging time reduction through multiple receiver coil data acquisition and image reconstruction,” *Magn. Reson. Med.* **29**(5), 681–687 (1993).

<sup>7</sup>J. B. Ra and C. Y. Rim, “Fast imaging using subencoding data sets from multiple detectors,” *Magn. Reson. Med.* **30**(1), 142–145 (1993).

<sup>8</sup>D. K. Sodickson and W. J. Manning, “Simultaneous acquisition of spatial harmonics (SMASH): fast imaging with radiofrequency coil arrays,” *Magn. Reson. Med.* **38**(4), 591–603 (1997).

<sup>9</sup>D. K. Sodickson, M. A. Griswold, and P. M. Jakob, “SMASH imaging,” *Magn. Reson. Imaging Clin. N. Am.* **7**(2), 1–18 (1999).

<sup>10</sup>D. K. Sodickson, “Tailored SMASH image reconstructions for robust *in vivo* parallel MR imaging,” *Magn. Reson. Med.* **44**(2), 243–251 (2000).

<sup>11</sup>K. P. Pruessmann, M. Weiger, M. B. Scheidegger, and P. Boesiger, “SENSE: Sensitivity encoding for fast MRI,” *Magn. Reson. Med.* **42**(5), 952–962 (1999).

<sup>12</sup>M. A. Griswold, P. M. Jakob, Q. Chen, J. W. Goldfarb, W. J. Manning, R. R. Edelman, and D. K. Sodickson, “Resolution enhancement in single-shot imaging using simultaneous acquisition of spatial harmonics (SMASH),” *Magn. Reson. Med.* **41**(6), 1236–1245 (1999).

<sup>13</sup>P. M. Jakob, M. A. Griswold, R. R. Edelman, and D. K. Sodickson, “AUTO-SMASH: A self-calibrating technique for SMASH imaging,” *MAGMA* **7**, 42–54 (1998).

<sup>14</sup>P. M. Jakob, M. A. Griswold, R. R. Edelman, W. J. Manning, and D. K. Sodickson, “Accelerated cardiac imaging using the SMASH technique,” *J. Cardiovasc. Magn. Reson.* **1**(2), 153–157 (1999).

<sup>15</sup>M. A. Griswold, P. M. Jakob, R. R. Edelman, and D. K. Sodickson, “A multicoil array designed for cardiac SMASH imaging,” *MAGMA* **10**, 105–113 (2000).

<sup>16</sup>J. A. Bankson, M. A. Griswold, S. M. Wright, and D. K. Sodickson, “SMASH imaging with an eight element multiplexed RF coil array,” *MAGMA* **10**, 93–104 (2000).

<sup>17</sup>D. K. Sodickson, C. A. McKenzie, W. Li, S. Wolff, W. J. Manning, and R.



- R. Edelman, "Contrast-enhanced 3D MR angiography with simultaneous acquisition of spatial harmonics: A pilot study," *Radiology* **217**(1), 284–289 (2000).
- <sup>18</sup> M. Weiger, K. P. Pruessmann, and P. Boesiger, "Cardiac real-time imaging using SENSE. SENSitivity Encoding scheme," *Magn. Reson. Med.* **43**(2), 177–184 (2000).
- <sup>19</sup> X. Golay, K. P. Pruessmann, M. Weiger, G. R. Crelier, P. J. Folkers, S. S. Kollias, and P. Boesiger, "PRESTO-SENSE: An ultrafast whole-brain fMRI technique," *Magn. Reson. Med.* **43**(6), 779–786 (2000).
- <sup>20</sup> R. F. Lee, C. R. Westgate, R. G. Weiss, and P. A. Bottomley, "An analytical SMASH procedure (ASP) for sensitivity-encoded MRI," *Magn. Reson. Med.* **43**(5), 716–725 (2000).
- <sup>21</sup> J. Wang and A. Reykowski, "A SMASH/SENSE related method using ratios of array coil profiles," in *Proceedings of the Seventh Scientific Meeting of the International Society for Magnetic Resonance in Medicine*, Philadelphia, PA (1999), p. 1648.
- <sup>22</sup> W. E. Kyriakos, L. P. Panych, D. F. Kacher, C. F. Westin, S. M. Bao, R. V. Mulkern, and F. A. Jolesz, "Sensitivity profiles from an array of coils for encoding and reconstruction in parallel (SPACE RIP)," *Magn. Reson. Med.* **44**(2), 301–308 (2000).
- <sup>23</sup> D. O. Walsh and A. F. Gmitro, "Sub-sampled phased-array MRI reconstruction via coherent spatial nulling," in *Proceedings of the Eighth Scientific Meeting of the International Society for Magnetic Resonance in Medicine*, Denver, CO (2000), p. 1720.
- <sup>24</sup> M. A. Griswold, P. M. Jakob, M. Nittka, J. W. Goldfarb, and A. Haase, "Partially parallel imaging with localized sensitivities (PILS)," *Magn. Reson. Med.* **44**(4), 602–609 (2000).
- <sup>25</sup> R. Heidemann, M. A. Griswold, A. Haase, and P. M. Jakob, "Variable density AUTO-SMASH imaging," in *Proceedings of the Eighth Scientific Meeting of the International Society for Magnetic Resonance in Medicine*, Denver, CO (2000), p. 274.
- <sup>26</sup> D. K. Sodickson, "A generalized basis approach to spatial encoding with coil arrays: SMASH-SENSE hybrids and improved parallel MRI at high accelerations," in *Proceedings of the Eighth Scientific Meeting of the International Society for Magnetic Resonance in Medicine*, Denver, CO (2000), p. 272.
- <sup>27</sup> R. Penrose, "A generalized inverse for matrices," *Proc. Cambridge Philos. Soc.* **51**, 406–413 (1955).
- <sup>28</sup> P. B. Roemer, W. A. Edelstein, C. E. Hayes, S. P. Souza, and O. M. Mueller, "The NMR phased array," *Magn. Reson. Med.* **16**(2), 192–225 (1990).
- <sup>29</sup> A. Ben-Israel and T. N. E. Greville, *Generalized Inverses: Theory and Applications* (Wiley, New York, 1977).
- <sup>30</sup> D. K. Sodickson, M. A. Griswold, P. M. Jakob, R. R. Edelman, and W. J. Manning, "Signal-to-noise ratio and signal-to-noise efficiency in SMASH imaging," *Magn. Reson. Med.* **41**(5), 1009–1022 (1999).
- <sup>31</sup> D. K. Sodickson, M. Stuber, R. M. Botnar, K. V. Kissinger, and W. J. Manning, "Accelerated coronary MRA in volunteers and patients using double-oblique 3D acquisitions with SMASH reconstruction," in *Proceedings of the Seventh Scientific Meeting of the International Society for Magnetic Resonance in Medicine*, Philadelphia, PA (1999), p. 1249.
- <sup>32</sup> H. M. M. Creemers and D. K. Sodickson, "Design of new receive coils for fast cardiac imaging," *J. Cardiovasc. Magn. Reson.* **1**, 278–279 (1999).
- <sup>33</sup> M. Stuber, R. M. Botnar, P. G. Danias, D. K. Sodickson, K. V. Kissinger, M. Van Cauteren, J. De Becker, and W. J. Manning, "Double-oblique free-breathing high resolution three-dimensional coronary magnetic resonance angiography," *J. Am. Coll. Cardiol.* **34**(2), 524–531 (1999).
- <sup>34</sup> R. M. Botnar, M. Stuber, P. G. Danias, K. V. Kissinger, and W. J. Manning, "Improved coronary artery definition with T2-weighted, free-breathing, three-dimensional coronary MRA," *Circulation* **99**(24), 3139–3148 (1999).
- <sup>35</sup> H. Azhari, D. K. Sodickson, R. R. Edelman, unpublished.
- <sup>36</sup> K. P. Pruessmann, M. Weiger, P. Boernert, and P. Boesiger, "Spiral SENSE: Sensitivity encoding with arbitrary  $k$ -space trajectories," in *Proceedings of the Seventh Scientific Meeting of the International Society for Magnetic Resonance in Medicine*, Philadelphia, PA (1999), p. 94.
- <sup>37</sup> K. P. Pruessmann, M. Weiger, P. Boernert, and P. Boesiger, "A gridding approach for sensitivity encoding with arbitrary trajectories," in *Proceedings of the Eighth Scientific Meeting of the International Society for Magnetic Resonance in Medicine*, Denver, CO (2000), p. 276.
- <sup>38</sup> S. A. R. Kannengiesser, A. R. Brenner, and T. G. Noll, "Accelerated image reconstruction for sensitivity encoded imaging with arbitrary  $k$ -space trajectories," in *Proceedings of the Eighth Scientific Meeting of the International Society for Magnetic Resonance in Medicine*, Denver, CO (2000), p. 155.